Lidar measurements of tropospheric water vapor and aerosol profiles over southeastern Italy

F. De Tomasi and M.R. Perrone
Istituto Nazionale di Fisica della Materia, Dipartimento di Fisica, via per Arnesano 73100 Lecce (Italy)

Abstract

A combined Rayleigh-Raman lidar based on a XeF excimer laser (351 nm) has been used for the regular monitoring of tropospheric aerosols and water vapor profiles over Southern Italy (40º 20'N, 18º 6' E), in the framework of the European Aerosol Research Lidar Network (EARLINET). Coincident measurements of vertical profiles of the aerosol backscattering ratio $R(z)$, the aerosol extinction coefficient $\alpha_{\lambda o}^{aer}(z)$, and the water vapor mixing ratio $w(z)$ have been performed during several months to investigate the correlation of $R(z)$ and $\alpha_{\lambda o}^{aer}(z)$ with water vapor and characterize the aerosol optical properties. A strong correlation has been found between the spatial and temporal evolution of $R(z)$ and $w(z)$ both in summer and in autumn regime. The experimental results have revealed that $R(z)$ increases with $w(z)$ and that the aerosol and water vapor burdens are lower in autumn than in the summer. The analysis of the data by using the 4-day analytical backward trajectories has revealed that the dependence of $\alpha_{\lambda o}^{aer}(z)$ and $R(z)$ on $w(z)$ is quite affected by the typical advection patterns over the lidar site. Aerosols providing a larger contribution to backscattering ratio and extinction coefficient as $w(z)$ increases have been monitored when air masses from North and East European Countries were advected over Lecce. The findings in terms of the lidar ratio S have revealed that aerosols with average S values ranging from 50 to 63 sr have been monitored when air masses from North and East Europe were advected over Lecce. On the contrary,

average *S* values ranging from 48 to 74 have been retrieved for air masses advected from North Africa.

1. Introduction

Water vapor and aerosols are two interesting atmospheric parameters that are generally monitored for the improved understanding of weather and climate (e. g. Ansmann et al., 1992; Charlson et al. 1992; King et al., 1992; Faizon et al.,1994; Hansen et al., 1997; International Panel on Climate Change (IPPC), 2001). Aerosols play an important role in the Earth's radiative balance and in the global climate, since they influence the radiation balance through two key processes: directly, by scattering and absorbing solar radiation, and indirectly, by acting as cloud condensation nuclei and thus dramatically affecting the optical properties of clouds (e. g**.** Holben et al., 1998; Torres et al., 1998; Ferrare et al., 1998; Haywood et al., 1999; Ferrare et al., 2001). The water vapor mixing ratio, on the other hand, is useful as a tracer of air parcel and in understanding energy transport mechanisms within the atmosphere (e. g. Whiteman et al., 1992; Ferrare et al., 2000). Indeed, water vapor is the key greenhouse gas in atmosphere and has an important role in radiation transfer processes, cloud formation, and atmospheric circulation (e. g. Bruegge et al.; 1992; Goldsmith et al., 1998). Moreover, water uptake significantly affects the particle size, shape, and chemical composition (e. g. Reichardt et al., 1996) and therefore the aerosol role in the radiative forcing of climate. Thus, simultaneous measurements of the vertical profiles of aerosols and water vapor densities are required to investigate the correlation between these two interesting atmospheric parameters (e. g. Kwon et al., 1997) and determinate the aerosol characteristics.

It has been shown in the last years, that lidar systems based on ultraviolet lasers, such as excimers, tripled, and quadrupled Nd-YAG lasers, are well-established tools for measuring

both water vapor and aerosols with high spatial and temporal resolution (e. g. Ferrare et al., 2000; Turner et al., 2002). We have used a combined Rayleigh-Raman lidar based on a XeF excimer laser (351 nm), for systematic monitoring of tropospheric aerosols and water vapor profiles at Lecce (40º 20'N, 18º 6' E), in the south-eastern corner of Italy. Lecce is located on the Salentum peninsula whose topography is quite flat. The Salentum peninsula is surrounded by two different seas (the Southern Adriatic and the Northern Ionian Sea) and the lidar station is located in a rural area at about 15 km from the Adriatic Sea and 25 km from the Ionian Sea. Nighttime Raman measurements of the vertical profiles of the aerosol backscattering ratio, the aerosol extinction coefficient, and the water vapor mixing ratio acquired between July and December 2000 are examined in the paper. The temporal and spatial relationship among the aerosol backscattering ratio and the water vapor mixing ratio in the troposphere is investigated. Attention is also given to the changes in the vertical distribution of $R(z)$ and of $w(z)$ as a result of the transition between summer and autumn regimes. Moreover, the 4-day analytical backward trajectories have been used to investigate how the correlation between these two important parameters depends on the typical advection patterns over the lidar site. Systematic and simultaneous measurements of $R(z)$ and $w(z)$ have seldom been reported, in spite of their important role for the improved understanding of weather and climate. The findings in terms of the extinction coefficient and lidar ratio values besides their dependence on water vapor mixing ratio and relative humidity, respectively, are also presented in the paper to better characterize the aerosol properties.

The experimental structure of the Rayleigh-Raman lidar and the analytical techniques applied for the determination of the atmospheric parameters are presented in Sect. 2 and 3, respectively. The measurements of $R(z)$ and $w(z)$ and the discussion on the determination of the aerosol characteristics from the relationship between $R(z)$ and $w(z)$, are reported in Sect. 4. The

analysis of the extinction and lidar ratio measurements is discussed in Sect. 5. The summary is given in Sect. 6.

2. Experimental Set-Up

A schematic set up of the lidar that utilizes a XeF excimer laser (Lambda Physik LPX 210 I) as radiation source, is shown in Fig. 1. The XeF laser emits light pulses of 30 ns duration at 351 nm, with a maximum energy and repetition rate of 250 mJ and 100 Hz, respectively. The expanded outgoing laser beam has a cross section of 40 x 25 mm^2 and an average divergence of 0.5 mrad. Collection of the backscattered radiation is obtained by a Newtonian telescope, whose primary mirror has 30 cm-diameter and 120 cm-focal length. The backscattered radiation is spatially filtered by a 4 mm-field stop aperture (A) located on the telescope focus and is monitored in three different channels. A double-grating monochromator (Jobin-Yvon DH10 UV) equipped with a 1 x 8 mm^2 slits and characterized by an out of band rejection better than 10^{-8}, is used in each channel to spectrally resolve the back-scattered radiation. No cross talk between nearby lines has been observed in the presence of dense water clouds (Reichardt et al., 1996) where elastic-to-Raman signal ratios are larger. The Raman signals are detected in the photon-counting regime. We use a photomultiplier (Ph) module Thorn EMI 9893B/350 to monitor the water vapor Raman signal at 403 nm and a Hamamatsu R1527 photosensor to monitor the nitrogen Raman signal at 383 nm. The photon counting chain is composed of a 300 MHz discriminator (Phillips Scientific Mod. 6908) and a multichannel scaler (EG&G MCS-Mod. 914 P). The elastic signal is monitored by a Hamamatsu R212UH photosensor and is acquired in both the analog-to-digital (A/D) and photon-counting modes. A LeCroy oscilloscope (Mod. 9361/C-300MHz) is used for the A/D acquisition. The MCS operates with a dwell time of 100 ns, yielding a spatial resolution of 15 m.

3. Theory

The aerosol backscattering ratio $R(\lambda_o, z)$ is used to quantify the ratio of aerosol to molecular scattering. It is equal to unity in a region of atmosphere that is free of aerosols and will exceed unity where aerosols are present. $R(\lambda_o, z)$ can be expressed in terms of the lidar signals as (e. g. Whiteman et al., 1992)

$$R(\lambda_0, z) = \frac{P_{N_2}(z_0) P_{\lambda_0}(z)}{P_{\lambda_0}(z_0) P_{N_2}(z)} \times \Delta T_R(z_0, z) \qquad (1)$$

where $P_{\lambda o}(z)$ denotes the return signal from distance z at the XeF laser wavelength λ_o, $P_{N2}(z)$ is the Raman nitrogen return signal from distance z and the aerosol-free height z_0 is chosen such that $\beta_{\lambda_0}^{aer}(z_0) + \beta_{\lambda_0}^{mol}(z_0) \cong \beta_{\lambda_0}^{mol}(z_0)$, where $\beta_{\lambda_0}^{mol}(z)$ and $\beta_{\lambda_0}^{aer}(z)$ denote the backscatter coefficient for Rayleigh and Mie scattering, respectively. $\Delta T_R(z, z_0)$ represents the transmission correction function and it is calculated by considering Rayleigh scattering and aerosol extinction. Absorption by ozone and other trace gases is negligible at these wavelengths (e. g. Whiteman et al., 1992). Radiosonde data of pressure and temperature are used to calculate air density profiles and the reduction in transmission due to Rayleigh scattering. In particular, we use radiosonde measurements that are performed by the italian weather service at the meteorological station of Brindisi (40° 39' N, 15° 57' E) every six hours. Brindisi is located 40 km north-west from the lidar site. The effect of particle optical thickness is estimated from the aerosol extinction coefficients derived from the measured N_2 Raman signal (e. g. Ansmann et al., 1992):

$$\alpha_{\lambda o}^{aer}(z) = \frac{d/dz\left\{\ln\left[N_2(z)/P_{N_2}(z)z^2\right]\right\} - \alpha_{\lambda_o}^{mol}(z) - \alpha_{\lambda_{N_2}}^{mol}(z)}{1 + (\lambda_o/\lambda_{N_2})^k} \qquad (2)$$

where $N_2(z)$ is the nitrogen molecular number density and $\alpha_{\lambda o}^{mol}$ and $\alpha_{N_2}^{mol}$ denote the extinction of light by atmospheric gas molecules at the wavelength λ_o and at the nitrogen Raman wavelength, respectively. λ^{-k} describes the wavelength dependence of the aerosol extinction, where the Angstrom coefficient k is a parameter which has to be guessed. $k = 1$ is normally assumed between 351 nm and 383 nm (Ansmann et al., 1990), even if the k value can vary depending on the size and composition of aerosols (Ferrare et al., 1998). We have assumed $k = 1$ and this assumption is further supported by the photometric measurements performed in Lecce by Borghesi (Borghesi et al., 1982). They have derived the Angstrom coefficient, obtaining values between 0.5 and 1.5, with an average k of 1.1. However, the ratio between emitted and Raman shifted wavelength is close to unity and deviations of this assumption do not contribute to significant errors (Ansmann et al.,1992; Ferrare et al., 1988; Whiteman, 1999).

In the data analysis it is assumed that the overlap function is unity in all channels at altitudes $z \geq 500$ m. This assumption is also supported by the results on the intercomparison campaign performed within the EARLINET project (Freudenthaler et al., 2002). However, a correction is applied to the backscattering ratio to account for the differences between overlap functions in each channel (e. g. Goldsmith et al., 1998). This correction is obtained with the elastic-channel monochromator tuned to the nitrogen wavelength so that both elastic and nitrogen channels observe return signals at the same wavelength. The ratio between the two overlap functions is then computed from the ratio of the return signals measured in these channels. Since both channels observe the same wavelength, this ratio does not depend on the atmospheric state and is therefore used to correct the measured backscattering ratio (Ferrare et

al., 1995). Application of this calibration procedure permits retrievals of backscattering ratio profiles down to about 150-300 m.

The determination of the particle extinction and backscatter coefficients implies, in addition, the determination of the extinction-to-backscatter ratio (lidar ratio):

$$S(z) = \alpha_{\lambda o}^{aer}(z) / \beta_{\lambda_0}^{aer}(z) \qquad (3)$$

The water vapor mixing ratio $w(z)$, is the mass of water vapor divided by the mass of dry air in a given volume and as a function of height can be expressed as

$$w(z) = K \frac{P_{H_2O}(z)}{P_{N_2}(z)} \times \Delta T_w(z) \qquad (4)$$

where K is the system calibration constant for water vapor mixing ratio measurements, $P_{H2O}(z)$ and $P_{N2}(z)$ are the Raman backscattered signals from water vapor and nitrogen, respectively and $\Delta T_w(z)$ is the transmission correction function for the water vapor mixing ratio (e. g. Ansmann et al., 1992). $\Delta T_w(z)$ is computed in a similar manner to that described above for the backscattering ratio. We have used in situ measurements of $w(z)$ taken at an altitude of 30 m to determinate the calibration factor K in Eq. 5. Radiosonde measurements were not available at the lidar site. However, it has been observed that the water vapor mixing ratio profiles monitored by the lidar at Lecce were in good accordance with the ones obtained at Brindisi by coincident radiosonde measurements. In fact, in flat regions, under stable meteorological conditions and in nights with vanishing wind speed, advective motions are not expected to occur and the water vapor distribution is expected to be rather homogeneous within places few ten of km away (De Tomasi et al., 2002). We believe that these intercomparisons provide

further confidence in the lidar calibration. As in the case of backscattering ratio, a correction is applied to Eq. (5) to account for the overlap function. To this end, the monochromator of the water vapor channel is tuned to the nitrogen wavelength so that both water vapor and nitrogen channels observe return signals at the same wavelength.

4. Determination of aerosol characteristics from the relationship between aerosol backscattering ratio and water vapor mixing ratio.

Lidar measurements of the backscattering ratio and of the water vapor mixing ratio acquired between July and December 2000 are examined in this section. They are the first measurements provided by a new lidar station that is located on a flat area (40º 20'N, 18º 6' E) rather close to European East Countries and North Africa. The measurements have been performed on a fixed schedule (twice a week) to get a statistically significant data set in accordance to the objectives of the European Project EARLINET (Bosenberg et al., 2001). Extra measurements have been done during Sahara dust events. The distribution of the lidar measurements is shown in Fig. 2; only the measurements acquired on days without clouds below 4 km have been considered. Measurement examples of the vertical profiles of the backscattering ratio (solid lines) and of the water vapor mixing ratio (dotted lines) are shown in Fig. 3. All lidar measurements have been taken one or two hours after the sunset time. In normal operation, data are recorded as 45 min profiles corresponding to the accumulation of signals from about 2 x 10^5 laser shots. The laser repetition rate was 80 Hz. The day and the average time (UT) during which the measurements have been performed are reported on the right side of each profile. Vertical averaging has been applied to $R(z)$ and $w(z)$. The window length was of 60 m for $R(z)$, whereas it was of 60 m below about 2 km and of 150 m above 2

km, for the water vapor mixing ratio profiles. The statistical uncertainties of $R(z)$ and $w(z)$ that have been calculated from the law of error propagation by assuming a Poisson noise on the lidar signals, are within 1-10% for $R(z)$ and 5-20% for $w(z)$ as it is revealed by the measurement examples of August 3rd and of July 27th, respectively, that are shown in Fig. 3. One observes from Fig. 3 that the spatial distributions of the backscattering ratio and of the water vapor mixing ratio are quite correlated. Indeed, the profiles of $R(z)$ and $w(z)$ are often characterized by similar vertical structures and the backscattering ratio gets close to one as the water vapor mixing ratio reaches values lower than 2g/kg, throughout all months.

The 4-day analytical back trajectories for the air parcels arriving over the lidar site at altitude up to about 4 km have been analyzed to investigate the relationship between $R(z)$ and $w(z)$, and air mass transport. The backscattering ratio was generally close to unity at altitude above 4 km for the lidar signals analyzed in this paper. The atmospheric backward trajectories have been calculated on a 3-dimensional grid with a time resolution of six hours, by the German Weather Service from the wind fields of the European numerical weather prediction model (Kottmeier and Fay, 1998). The accuracy of the calculated trajectories depends on the synoptic conditions. The higher the wind-speed the lower the uncertainty of the trajectories. Usually the deviation between the calculated and the actual track of an air parcel is about 10% to 20% of the trajectory length for the trajectories used in this study (Stohl, 1998). The data are provided for six distinct arrival height levels (975, 850, 700, 500, and 200 hPa) and for two arrival times (13:00 UT and 19:00 UT) on a day–by-day basis. The analysis of the advection patterns over the lidar site for the days listed in Fig. 2 has revealed that these days and hence the corresponding lidar measurements can be divided into three main clusters by considering the air parcel origin. The days characterized by diverging advection patterns up to 4 km have not been considered. In the first cluster we have grouped all measurements performed on days

characterized by advection patterns coming from the European Countries located at latitudes larger than 40°. These days are marked in Fig. 2 by full dots. Typical 4-day backward trajectories for the arrival of North and East-Europe air masses at Lecce are shown in Fig. 4a and 4b, respectively. The vertical profiles of $R(z)$ and $w(z)$ that have been monitored in Lecce under the advection patterns of Fig. 4 are given in Fig. 3. One observes from Fig. 4 that the air masses coming from North and East Europe have the common property to travel across several industrialized European areas before reaching Lecce. Therefore, these air masses can all be quite affected by anthropogenic aerosols. Depending on travel distance and residence time over the source regions, the particle number concentrations, the physical and chemical state, and thus the optical properties of the aerosols change.

All measurements performed on days characterized by advection patterns coming from regions located at latitudes lower than 40° have been grouped in the next two clusters. In particular, all measurements performed on days characterized by advection patterns coming from the Mediterranean and Atlantic Sea have been grouped in one cluster. These days are marked in Fig. 2 by open boxes. Figure 5a shows typical 4-day back trajectories for the arrival at Lecce of Atlantic air masses. We believe that mainly "maritime" type aerosols are transported at Lecce by these last advection patterns. These air masses can be less affected by anthropogenic aerosols along the way to Lecce, since they may cross only some lands of South of Spain before reaching Italy. However, over the oceans, the occurrence of the sea salt components is mainly limited to the PBL. Above PBL, the aerosol composition is expected to be similar to that of continental aerosol but with small amount of insoluble particles (Ackermann, 1998, Ansmann et al., 2001).

In the last cluster all measurements performed on days characterized by advection patterns coming from North Africa have been grouped, since they mainly transport "desert"

type aerosols over Lecce (Fig. 5b). These days are marked by full boxes on Fig. 2. The vertical profiles of $R(z)$ and $w(z)$ that have been monitored in Lecce under the advection patterns shown in Fig. 5 are given in Fig. 3.

It is worth mentioning that the time difference between the arrival time of the back trajectories and the average time during which lidar measurements have been performed is not more than two hours. We believe that this time difference does not significantly affect the sampling of the clusters by considering the wide geographical extension of each cluster besides the accuracy and the resolution time of the calculated trajectories. Moreover, lidar measurements have generally been performed under locally stable meteorological conditions and we have not observed significant variations of the measured parameters within 2-3 hours.

The backscattering ratio and water vapor measurements have then been grouped into three main clusters, in accordance to the advection pattern analysis presented above, to investigate their correlation besides their dependence on air mass transport. Figure 6 shows the scatterplot of the backscattering ratio versus the water vapor mixing ratio, for the measurements performed on days characterized by advection patterns coming to Lecce from (a) the European Countries located at latitudes larger than 40^{o} (Fig. 2, full dots), (b) the Mediterranean and Atlantic Sea (Fig. 2, open boxes), and (c) North Africa (Fig. 2, full boxes). Only independent data points have been plotted in Fig. 6. One observes from Fig. 6 that backscattering ratio and water vapor mixing ratio are quite correlated and that $R(z)$ increases with $w(z)$ for all advection patterns. A simple linear functional relationship has been used to infer the dependence of $R(z)$ on $w(z)$ and one observes that the slope obtained by fitting the data of Fig. 6a is about twice that obtained by fitting the data of Figs. 6b and 6c, respectively. So, $R(z)$ increases faster with water vapor mixing ratio for the air masses advected from North and East Europe. The larger sensitivity of $R(z)$ to water vapor changes revealed by Fig. 6a can

be ascribed to a larger presence of anthropogenic aerosols. The residence time of the air masses over industrialized and polluted lands may lead to an increase of the aerosol load and then of the backscattering ratio. However the larger increase of $R(z)$ with $w(z)$ can be due to a larger presence of aerosols providing higher backscatter signals at 351 nm as $w(z)$ increases. Water uptake leads to an increase of the particle size and the 180° backscatter is very sensitive to particle size changes: light scattering efficiency is roughly proportional to the particle cross section (Ansmann et al., 2001). Fitzgerald (1984) has analytically investigated at 0.694 and 10.6 μm, the effect of relative humidity on the aerosol backscatter coefficient. He has found that an increase in the volume fraction of water-soluble material (Ackermann, 1998) resulted in an increase in the sensitivity of the backscatter coefficient to changes in relative humidity. He has also found that at 0.694 μm, the sensitivity of the backscatter coefficient to changes in relative humidity was greater when soot was uniformly mixed with the water-soluble and dustlike materials than when the same amount of soot was present as individual particles. Water soluble and soot are the main components of continental aerosols besides insoluble particles (Ackermann, 1998). The lower sensitivity of $R(z)$ to $w(z)$ changes revealed by Fig. 6c can be ascribed to a large presence of "desert" type aerosols that are advected over Lecce from North Africa. Desert dust has a broad particle size spectrum, it mainly consists of minerals and no dependence on water vapor has generally been considered for this type of aerosols (Barnaba et al., 2001) because of their non hygroscopic behavior (Li et al., 1998).

The seasonal dependence of the aerosol and water vapor load observed at Lecce from the measurements acquired between July and December 2000 has also been analyzed. The profiles of Fig. 3 show that $R(z)$ and $w(z)$ values are generally smaller as a result of the transition between summer and autumn regimes, and that the aerosol and water vapor burdens are on the average, lower in autumn than in summer. The aerosol integrated backscatter I_B and

the water vapor columnar content C_w between 500 m and 4000 m have been calculated to better infer the seasonal dependence of the aerosol and water vapor load revealed by Fig. 2. Figure 7 shows (a) I_B (open dots) and (b) C_w (open boxes) as a function of time. The heights at which the aerosol and water vapor load reduce to a significantly low value, R^* and w^*, respectively, have also been determined to infer the time evolution of the aerosol and water vapor burdens. It is possible to see from Fig. 6 that, in the considered altitude range, $R(z)$ varies between 1 and 2.6 and $w(z)$ between 0 and 12 g/kg. We have chosen R^* and w^* by adding 20% of the total variation range to the corresponding minimum value of $R(z)$ and $w(z)$, respectively. Figure 7a (full dots) shows, as a function of time, the altitudes at which the backscattering ratio value reduces to R^*=1.3. Whereas, Fig. 7b (full boxes) shows as a function of time the altitudes at which the water vapor mixing ratio reduces to w^*=2.4 g/kg. One clearly observes from Fig. 7a either that I_B reduces of about 50% as a result of the transition between summer and autumn regime, and that the aerosol on the average are confined to lower altitudes from October to December 2000. A similar spatial and temporal evolution is revealed for water vapor by Fig. 7b. Routine measurements of the aerosols vertical profiles performed by a Raman lidar at Southern Great Plains (USA) during 1998 and 1999, have also revealed that the aerosol optical thickness was generally higher in summer and lower in winter (Turner et al., 2001). We believe that the seasonal change of the observed vertical distribution of the backscattering ratio, can be ascribed to the different growth of the planetary boundary layer (PBL) that occurs as a result of the transition between summer and autumn regimes (Matthias and Bosenberg, 2002). Aerosols tend to be trapped within the PBL and can be used as tracers for the study of the boundary-layer vertical structure and time variability (Flamant et al., 1997). In summer times and under clear sky conditions, the growth of the PBL during the day hours is favored by the larger solar flux and this allows a larger aerosol

penetration in the mixed layer throughout the day and the aerosol persistence in the residual layer at night. Then, in absence of advection a clear change in aerosol concentration appears evident at the top of the residual layer, in the former entrainment zone, rather than at the top of the stable surface layer (Santacesaria et al., 1998). Moreover, the weather stability typical of summer regimes favors the persistance of these structures.

5. Aerosol characterization by extinction and lidar ratio measurements.

The aerosol extinction coefficient has been calculated from a linear fit of the logarithm of the nitrogen Raman signal, to obtain its derivative with respect to range (4), on a window length that was generally about 150 m below 1.5 km and 450 m above 1.5 km As it is well known, only the Raman lidar and the high spectral resolution technique allow the measurement of reliable aerosol extinction profiles by lidar systems (Ansmann et al., 1992; Grund et al., 1991). As it has been mentioned, the determination of the particle extinction and backscatter coefficient allows a better characterization of the aerosol properties by means of the extinction-to-backscatter ratio (Sasano and Browell, 1989; Ackermann, 1998**;** Barnaba and Gobbi, 2001, Matthias and Bosenberg, 2002). The lidar ratio $S(z)$ depends on size distribution, shape and chemical composition (refractive index) of the particles and it generally increases with decreasing particle size and increasing contribution of absorption to light extinction (Ansmann et al., 2001). Literature values of $S(z)$ range from about 10 to 150 sr (e.g. Barnaba and Gobbi, 2001, Matthias and Bosenberg, 2002). Lidar ratios ranging from 51 to 57 sr have been assumed by Sasano and Browell (1989) to get trustworthy backscatter profiles at 300 nm, from measurements in lofted Saharan dust layers near Barbados. By contrast, they have proposed a value of S of 36 sr at 300 nm, as representative of rural continental aerosols. In the numerical study performed by Ackermann (1998) the lidar ratios have been calculated for continental,

maritime, and desert aerosols. It has been found at 355 nm that for continental aerosol, S increases with the relative humidity from 42 to 70 sr, whereas lies between 17 and 24 sr for maritime aerosol. A weak dependence of S on relative humitity has been observed for desert aerosol, in fact it has been found that S ranges between 42 and 48 sr for 355 nm**.**

The profiles of $S(z)$ in this paper are computed using the aerosol extinction and backscatter coefficient profiles, and therefore the backscatter profiles are smoothed to match the resolution of the aerosol extinction profiles before computing $S(z)$. Measurement examples of the vertical profiles (a) of the aerosol extinction $\alpha_{\lambda o}^{aer}(z)$, (b) of the backscatter coefficient $\beta_{\lambda_0}^{aer}(z)$ (solid line) and relative humidity $RH(z)$ (dotted line), and (c) of the lidar ratio $S(z) = \alpha_{\lambda o}^{aer}(z)/\beta_{\lambda_0}^{aer}(z)$ that have been retrieved by the lidar measurements of August 3rd are shown in Fig. 8. The relative humidity profile has been derived from the water vapor mixing ratio lidar data and the temperature profiles from the radiosonde measurements performed in Brindisi (Ansmann et al., 1992; Ferrare et al., 2001). Temperature radiosonde measurements were not available at the lidar site. However, the temperature vertical profile is expected to be rather homogeneous within places few ten of km away in flat regions, at night time, and under stable meteorological conditions (De Tomasi et al., 2002).

The lidar profiles of Fig. 8 reveal the presence of different air masses between 400-3300 m, especially in terms of the lidar ratio. One observes that the lowermost layer is characterized by lidar ratios of about 30 sr. Lidar ratios of about 40 sr are found between 700-1800 m whereas, above 1800 m the lidar ratios vary between 40 and 60 sr. The smaller values of the backscatter coefficient and the larger values of the lidar ratios above 1800 m may indicate a larger presence of small, considerably absorbing particles above 1800 m (Ansmann et al., 2001). Lidar ratios of 40 sr between 700-1800 m may indicate less absorbing (clean

continental, rural) particles (Ackermann, 1998) or mixtures of marine and continental aerosols (Ansmann et al., 2001). Whereas, the lidar ratios of about 30 sr measured below 700 m may be ascribed to a larger presence of marine particles. For large, marine particles the lidar ratio is expected to be in the range 17 to 24 at 355 nm (Ackermann, 1998). The 4-day backward trajectories of August 3rd (Fig. 4a) appear to support the above comments. Figure 4a reveals that air masses coming from the North Sea and Central Europe reach Lecce on August 3rd. They cross several polluted areas before reaching the lidar site and as a consequence are characterized by lidar ratio values that are typical of "continental" type aerosols (Ackermann, 1998). However, the lowermost layer is quite close to the Adriatic Sea surface in the last 24 hours before reaching Lecce and may be, as a consequence we have found that the lidar ratio reduces with altitude and reaches values of 30 sr below 700 m.

The correlation between extinction coefficient and water vapor measurements besides the dependence on air mass transport has also been investigated. To this end, the extinction coefficient and water vapor mixing ratio measurements have also been grouped into three main clusters depending on the origin of the air masses advected over the lidar site. It has been found that the extinction coefficient increases with water vapor for all advection patterns. But, the sensitivity of $\alpha_{\lambda o}^{aer}(z)$ to water vapor changes was larger for the air masses advected from the North and East European Countries located at latitudes larger than 40^{o} (Fig. 2, full dots) as it has been found for the backscattering ratio (Fig 6). This last result can be ascribed to a larger presence of particles whose contribution to light extinction increases faster as the water vapor mixing ratio gets larger.

Finally, the lidar ratio values obtained from the extinction and backscatter coefficient measurements acquired between July and December 2000 have been analyzed. The $S(z)$ values have been plotted as a function of the relative humidity RH to better compare our data with

those reported in literature. The *RH* effects on the chemical and microphysical aerosol properties have recently been investigated by Ackermann (1998). He has shown that the *RH* effects depend on the aerosol origin and as a consequence the dependence of lidar ratio on relative humidity allows a better characterization of aerosols. Figure 9 gives the lidar ratio values (symbols) versus *RH* for the measurements acquired on days characterized by advection patterns coming from (a) the European Countries located at latitudes larger than 40° (Fig. 2, full dots), (b) the Mediterranean and West Atlantic Sea (Fig. 2, open boxes), and (c) North Africa (Fig. 2, full boxes). The average value (symbols), the ±1 standard error (SE) of the mean (inner bars), and the ±1 standard deviation of the lidar ratio measurements (outer bars) are shown in Fig. 9, for 6 *RH* intervals. The outer error bars in Fig. 9 reveal the variability range of the lidar ratio values, being the atmospheric aerosols characterized by quite different chemical and morphological properties (Barnaba and Gobbi, 2001). The lidar ratio, besides its dependence on *RH,* is also rather dependent on the mixing ratio combination of the different aerosol components and the simultaneous existence of different aerosol types in different heights can lead to a large spread of the *S* values (Ackermann, 1998). The dashed, dotted and solid lines plotted in Fig. 9 show *S* versus *RH* for a "continental", "desert", and "maritime" aerosol type, respectively, as modeled by Ackermann (1998).

One observes from Fig. 9a that the average lidar ratio values (full dots) show a small trend to increase with increasing *RH.* This trend can be due to a decrease in both the real and imaginary part of the refractive index as well as a shift in the particle size distribution toward larger particles (Ferrare et al., 2001). Moreover, Fig. 9a reveals that the dependence of the average lidar ratio values (full dots) on *RH* appears to be quite consistent to that for a "continental" aerosol type (dashed line) for the air masses advected from the European Countries located at latitudes larger than 40°. Smaller average lidar ratio values ranging from

23 to 44 sr have been retrieved from the lidar measurements acquired when air masses from the West Atlantic and Mediterranean Sea were advected over Lecce as it is revealed by Fig. 9b (open boxes). One expects that "maritime" type aerosols are mainly transported by the last mentioned advection patterns. However, over the Oceans, the occurrence of the sea salt components is mainly limited to the PBL. Above PBL, the aerosol composition is expected to be similar to that of continental aerosol (Ansmann et al., 2001) but with small amount of insoluble particles (Ackermann, 1998). Moreover, the air masses arriving from the Atlantic and Mediterranean Sea could be affected by anthropogenic aerosols if they cross some polluted Spanish and/or Italian areas before reaching Lecce. As a consequence Fig. 9b reveals that the measured average lidar ratio values (open boxes) are generally larger than the values of the curve (solid line) that shows *S* versus *RH* for a "maritime" aerosol type as modeled by Ackermann (1998).

Figure 9c shows that average lidar ratio values ranging from 48 to 74 sr have been retrieved from the lidar measurements acquired when air masses from North Africa were advected over Lecce, whereas lidar ratios ranging from 42 to 47 sr at 355 nm have been obtained for desert dust aerosols from the numerical study based on the Mie theory that has been performed by Ackermann (1998). We believe that the non spherical shape of the desert type particles is responsible of the larger experimental *S* values of Fig. 9c (full boxes). Particle shape besides particle size can affect the *S* value. In fact, it has been shown by Mishchenko (Mishchenko et al., 1996) that for polydisperse systems of irregular particles the *S* values can be 1.5-3 times larger than the values associated with similar sized spherical particles, provided that the particle size is larger than some characteristic size. To this end it is worth mentioning that the numerical model developed by Barnaba and Gobbi (2001) has provided lidar ratio values ranging from 35 to 50 sr at 532 nm for non spherical dust aerosols. Lidar ratio values

varying from 20 to 25 sr at 532 nm have instead been reported by Ackermann (1998). Unexpectedly large lidar ratios, mainly between 60 and 100 sr at 355 nm have recently been observed in dust layers by Mattis et al. (2002) over Leipzig (Germany). The long-range transport that leads to an efficient removal of coarse mode particles with diameter > 1μm by gravitational settling and the non spherical shape of the particles have been considered responsible for the large Sahara dust lidar ratio values.

6. Summary and conclusion

Coincident measurements of tropospheric aerosol and water vapor profiles acquired from July to December 2000 at Lecce (40° 20' N, 18° 6' E) by a Rayleigh-Raman lidar have been presented and analyzed. These are the first measurements provided by a new lidar station that is located on a flat rural area at about 15 km from the Adriatic Sea and at 25 km from the Ionian Sea, and which is rather close to European East Countries and North Africa

The investigation of the temporal and spatial relationship among the aerosol backscattering ratio and the water vapor mixing ratio, besides some preliminary results on the optical characterization of the observed aerosols, were the main goals of the paper. The analysis of the lidar data has revealed a strong correlation between the spatial and temporal evolution of $R(z)$ and $w(z)$ both in summer and in autumn regimes. It has been found that $R(z)$ increases with $w(z)$ and that both reduce as a result of the transition between summer and autumn regime. This last result is clearly revealed by Fig. 7 that shows the temporal evolution of the water vapor column content and of integrated aerosol backscatter coefficient from summer to autumn, besides the altitudes at which the backscattering ratio reduces to 1.3 and $w(z)$ reduces to 4 g/kg. It has also been observed that the correlation among $R(z)$ and $w(z)$ was dependent on the air masses origin. Indeed, the sensitivity of the scattering ratio to water vapor

changes was larger for the air masses advected from North and East European Countries (Fig 6). The larger increase of $R(z)$ with $w(z)$ revealed by Fig. 6a has been ascribed to a larger presence of aerosols for which the shift in the particles size distribution toward larger particles was larger as $w(z)$ increases. The correlation among $\alpha_{\lambda o}^{aer}(z)$ and $w(z)$ was also dependent on the air masses origin. $\alpha_{\lambda o}^{aer}(z)$ increases with $w(z)$ but, the sensitivity of the extinction coefficient to water vapor changes was also larger for the air masses advected from the North and East European Countries. This last result has been ascribed to a larger presence of particles whose contribution to light extinction increases more with water vapor. So, aerosols providing a larger contribution to the backscattering ratio and to the extinction coefficient as $w(z)$ increases, have been monitored when air masses coming from the European Countries located at latitudes larger than 40° were advected over Lecce. The findings in terms of the dependence of the lidar ratio with relative humidity have revealed that S shows a small trend to increase with RH. Aerosols with average lidar ratio values ranging from 50 to 63 sr have been monitored when air masses from North and East European Countries were advected over Lecce (Fig. 9a), and the dependence of S on RH for these aerosols appears to be consistent to that for a "continental" aerosol type as modeled by Ackermann (1998). Average lidar ratio values ranging from 23 to 44 sr have instead been found for the air masses advected over Lecce from the West Atlantic and Mediterranean Sea (Fig. 9b). Largest lidar ratio values ranging from 48 to 74 sr (Fig. 9c) have been found for the advection patterns coming from North Africa. The non spherical shape of the dust particles can mainly be considered responsible of the high S values shown in Fig. 9c (full boxes).

We believe that the results given in the paper have provided a preliminary characterization of the aerosol properties by considering the main advection patterns over the

lidar site. These results may be useful for a proper consideration of aerosols and water vapor mixing ratios in global climate models. Vertical aerosol and water vapor profiles are required for a proper interpretation of data from ground-based and space-based radiometers.

Acknowledgements

This work was supported by the Environment Program of the European Union, Under the contract EVR1-CT1999-40003. Air-mass trajectory analysis was performed by the German Weather Service (DWD), by using an IDL code provided by I. Mattis (IFT, Germany). The radiosounding data of the meteorological station of Brindisi (Italy) have been provided by NOAA (http://raob.fsl.noaa.gov).

References

Ackermann J., The Extinction-to-Backscatter Ratio of Tropospheric Aerosol: A Numerical Study, *J. of Atm. And Oceanic Techn., 15*, 1044-1050, 1998.

Ansmann A., M. Riebesell, and C. Weitkamp, Measurement of atmospheric aerosol extinction profiles with a Raman lidar,*Opt. Lett.,15*, 746-748, 1990.

Ansmann A., M. Riebesell, U. Wandinger, C. Weitkamp, E. Voss, W. Lahmann, and W. Michaelis, Combined Raman Elastic-Backscatter LIDAR for Vertical Profiling of Moisture, Aerosol Extinction, Backscatter, and LIDAR Ratio, *Appl. Phys., B55*, 18-28,1992.

Ansmann A., F. Wagner, D. Althausen, D. Muller, A. Herber, and U. Wandinger, European Pollution Outbreaks during ACE 2, Part I: Alofted Aerosol Plumes observed with Raman Lidar at the Portuguese Coast, *J. Geophys. Res*., 106 D, 20723-20733, 2001.

Barnaba F., G. P. Gobbi, Lidar estimation of tropospheric aerosol extinction, surface area, and volume: Maritime and desert-dust cases, *J.of Geophys. Res.*, 106 d,3005-3018, 2001.

Borghesi A., E. Bussoletti, G. Falcicchia, and A. Minafra, Determination of atmoepheric precipitable water vapour and turbidity parameters from diurnal infrared hygrometer and turbidimeter data, *Infrared Phys., 22*, 149-155, 1982.

Bosenberg J., et al., EARLINET:A European Aerosol Research lidar Network, In *Advances in Laser Remote Sensing*, edited by A. Dabas, C. Loth, and J. Pelon, pp. 155-158, Ecole Polytechnique, Palaiseau, France, 2001.

Bruegge, C. T., J. E. Conel, R. O. Green, J. S. Margolis, R. G. Holm, and G. Toon, Water vapor column abundance retrievals during FIFE, *J. Geophys. Res., 97,*18,759-18,768, 1992.

Charlson R. J., S. E. Schwartz, J. M. Hales, R. D. Cess, J. A. Coakley Jr., J. E. Hansen, and D. J. Hofmann, Climate forcing by anthropogenic aerosol, *Science, 255,*423-430, 1992.

De Tomasi, P. Martano, M. Miglietta, A. Morabito, and M. R. Perrone, Lidar Monitoring of Water Vapor and Comparison with Meteorological Simulations, submitted *Il Nuovo Cimento C* (2002).

Faizon, C. A., A. Podaire, and G. Dedieu, Monitoring of Sahelian aerosol and armospheric water vaporcontent characteristics from sun-photometer measurements, *J. Appl. Meteorol., 33,*1291-1304, 1994.

Ferrare R. A., S. H. Melfi, D. N. Whiteman, K. D. Evans, F. J. Schmidlin, and D. O'C. Starr, A comparison of water vapor Measurements Made by Raman Lidar and Radiosondes, *J. of Atm. and Oceanic Technology, 12,*1177-1195, 1995.

Ferrare R. A., S. H. Melfi, D. N. Whiteman, K. D. Evans, R. Leifer, Raman lidar measurements of aerosol extinction and backscattering 1. Methods and comparison, *J. of Geophys. Res, 103,*19663-19672, 1998.

Ferrare R. A., S. Ismail, E. Browell, V. Brackett, M. Clayton, S. Kooi, S. H. Melfi, D. Whiteman, G. Schwemmer, K. Evans, P. Russell, J. Livingston, B. Schmid, B. Holben, L. Remer, A. Smirnov, and P. V. Hobbs, Comparison of aerosol optical properties and water vapor among ground and airborne lidars and Sun photometers during TARFOX, *J. of Geophys. Res., 105,*9917-9933, 2000.

Ferrare R. A., D. D. Turner, L. Heilman Brasseur, W. F. Feltz, O. Dubovik, and T. P. Tooman, Raman lidar measurements of the aerosol extinction-to-backscatter ratio over the Southern Great Plains, *J. of Geophys. Res.,106,*20333-20347, 2001

Flamant C., J. Pelon, P. H. Flamant, and P. Durand, Lidar Determination of the entrainment zone thickness at the top of the unstable marine atmospheric boundary layer, *Boundary-layer Meteorology*, *83*, 247-284, 1997.

Freudenthaler V. et al., Intercomparison of 21 aerosol lidar system in the frame of EARLINET, in "Lidar Remote Sensing in Atmosphere and Earth Science", Proc. Of

the XXI International Laser Radar Conference, Quebec, Canada, 8-12 July 2002, L. R. Bissonette, G. Roy, and G. Valle Editors.

Goldsmith J. E. M., Blair F. H., Bisson S. E., and Turner D.D., Turn-key Raman lidar for profiling atmospheric water vapor, clouds, and aerosol*, Appl. Optics, 37*, 4979-4990, 1998.

Grund C. J. and E. W. Eloranta, The University of Wisconsin High Spectral Resolution Lidar, *Optical Engineering, 30,* 6-12, 1991.

Hansen, J., M. Sato, and R. Ruedy, Radiative forcing and climate response, *J. Geophys. Res., 102,*6831-6864, 1997.

Haywood, J. M., V. Ramaswamy, and B. J. Soden, Tropospheric aerosol climate forcing in clear-sky satellite observations over the oceans, *Science, 283,* 1299-1303, 1999.

Holben, B. N., et al., AERONET-A federal instrument network and data archive for aerosol characterization, *Remote Sens. Environ., 66,*1-16, 1998.

IPCC (Intergovernmental Panel of Climate Change), 2001: Climate Change 2001. The scientific basis. Eds. J. T. Houghton, Y. Ding, M. Nogua, D. Griggs, P. Vander Linden, K. Maskell, Cambridge Univ. Press., Cambridge, U. K. (in press).

King, M. D., Y. J. Kaufman, W. P. Mezel, and D. Tanre, Remote sensing of cloud, aerosol, and water vapor properties from the Moderate Resolution Imaging Spectrometer (MODIS), *IEEE, Trans. Geosci. Remote Sens., 30,* 2-27, 1992.

Kottmeier C. and B. Fay, Trajectories in the antartic lower troposphere, *J. Geophys. Res.,105,* 10947-10959, 1998

.

Kwon S. A., Iwasaka Y., Shibata T., and Sakai T., Vertical Distribution of Atmospheric Particles and Water Vapor Densities in the Free Troposphere: Lidar Measurements in Spring and Summer in Nagoya, Japan, *Atm. Environ.,31*, 1459-1465, 1997.

Li, X., H. B. Maring, and J. M. Prospero, Effects of relative humidity on light scattering by mineral dust as measured in the marine boundary layer over the tropical Atlantic Ocean, *J. Geophys. Res.,* 103, 31,113-31,121, 1998.

Matthias V. and J. Bosenberg, Aerosol climatology for the planetary boundary layer derived from regular lidar measurements, *Atm. Research, 63,* 221-245, 2002.

Mattis I., A. Ansmann , D. Muller, U. Wandinger, and D. Althausen, "Dual-wavelength Raman lidar observations of the extinction-to-backscatter ratio of Sahara dust, " *Geophys. Res. Lett., 29* , 2002.

Reichardt J., Wandiger U., Serwazi M., and Weitkamp C., Combined Raman Lidar for Aerosol, Ozone, and Moisture Measurements, *Opt. Eng., 35*, 1457-1465, 1996.

Santacesaria V., Marenco F., Balis D., Papayannis A., and Zerefos C., Lidar Observation of the Planetery Boundary Layer above the city of Thessaloniki, Greece, *Il Nuovo Cimento, 21*, 585-596, 1998.

Sasano Y. And Browell E. V., Light Scattering Characteristics of Various Aerosol Types Derived from Multiple Wavelength Lidar Observations, *Appl. Optics 28*, 1670-1679, 1989.

Stohl A., Computation, accuracy and application of trajectories-a review and bibliography, *Atmos. Environ., 32,*947-966, 1998.

Torres, O., P. K. Bhartia, J. R. Herman, Z. Ahmad, and J. Gleason, Derivation of aerosol properties from satellite measurements of backscattered ultraviolet radiation: Theoretical basis, *J. Geophys. Res., 103,* 17,099-17,110, 1998.

Turner D. D., R. A. Ferrare, L. H. Brasseur, Average aerosol extinction and water vaporprofiles over the Southern Great Plains, *Geophys. Res. Letters, 28,*4441-4444, 2001.

Turner, D. D., R. A. Ferrare, L. A. Heilman, W. F. Feltz, and T. Tooman, Automated retrievals of water vapor and aerosol profiles over Oklahoma from operational Raman lidar, *J. Atmos. Oceanic Tech., 19,*37-50, 2002.

Whiteman, D. N., Application of statistical methods to the determination of the slope in lidar data, *Appl. Optics 38*, 3360-3369, 1999.

Whiteman D. N., S. H. Melfi, and R. A. Ferrare, Raman Lidar System for the Measurement of Water and Aerosol in the Earth's Atmosphere, *Appl. Optics, 31*, 3068-3082, 1992.

Figure Captions

Fig. 1 Schematic set-up of the XeF based Rayleigh-Raman Lidar: A, aperture; L1, collimating lens; D, dichroic mirror; L, focusing lens; M_n, monochromator; Ph, Photosensor; Q, quartz beam splitter; F, neutral density filters; Disc, dicriminator; MCS, multi channel scaler.

Fig. 2 Distribution of the lidar measurements acquired between July and December 2000 on days without clouds below 4 km. The measurements acquired on days characterized by advection patterns coming from the European Countries located at latitudes larger than 40° are marked by full dots. Open boxes mark the days characterized by advection patterns coming from the Atlantic Ocean and Mediterranean Sea. Full boxes mark the days characterized by advection patterns coming from North Africa.

Fig. 3 Examples of the 45-minute average profiles of the aerosol scattering ratio (solid line) and of the water vapor mixing ratio (dotted line), acquired between July and December 2000. The day and the average time (UT) during which measurements have been performed are reported on the right side of each profile. Typical statistical uncertainties of $R(z)$ and $w(z)$ that have been calculated from the law of error propagation by assuming a Poisson noise on lidar signals are shown on the scattering ratio profile of August 3rd and on the water vapor mixing ratio profile of July 27th.

Fig. 4 Typical 4-day backward trajectories for discrete arrival pressure levels, for the 19:00 (UT) arrival time, and for the arrival at Lecce of (a) North Europe, and (b) East-Europe air masses.

Fig. 5 Typical 4-day backward trajectories for discrete arrival pressure levels, for the 19:00 (UT) arrival time, and for the arrival at Lecce of (a) Atlantic Ocean and Mediterranean Sea, and (b) North Africa air masses.

Fig. 6 Scatterplot of the backscattering ratio versus the water vapor mixing ratio for the measurements performed on days characterized by advection patterns coming from (a) European Countries located at latitudes larger than 40°, (b) Atlantic Ocean and Mediterranean Sea and (c) North Africa. The solid line is the linear least square best fit to the data.

Fig. 7 Temporal evolution from July to December 2000 of (a) the aerosol integrated backscatter coefficient between 500 m and 4000 (open dots) and of the altitude at which the backscattering ratio value reduces to 1.3 (full dots), and of (b) the water vapor column content between 500 m and 4000 (open boxes) and the altitude at which the water vapor mixing ratio reduces to 4g/kg (full boxes).

Fig. 8 45-minute average profiles (a) of the aerosol extinction coefficient, (b) of the aerosol backscatter coefficient (solid line) and of the relative humidity (dotted line), and (c) of the lidar ratio, measured on August 3rd. Error bars indicate one standard deviation caused by statistical errors. The date and the average time

(UT) during which measurements have been performed are reported in the box on the left side of the figure.

Fig. 9 Plot of the lidar ratio data versus the relative humidity *RH* for the measurements performed on days characterized by advection patterns arriving at Lecce from (a) European Countries located at latitudes larger than 40°, (b) Atlantic Ocean and Mediterranean Sea, and (c) North Africa. The average value (symbols), the ± 1 SE of the mean (inner bars), and the ±1 standard deviations (outer bars) of the lidar ratio measurements are given for six *RH* intervals. *S* as modeled by Ackerman (1998) for continental (dashed line), desert (dotted) and maritime (solid line) aerosols is also shown in Fig. 9.

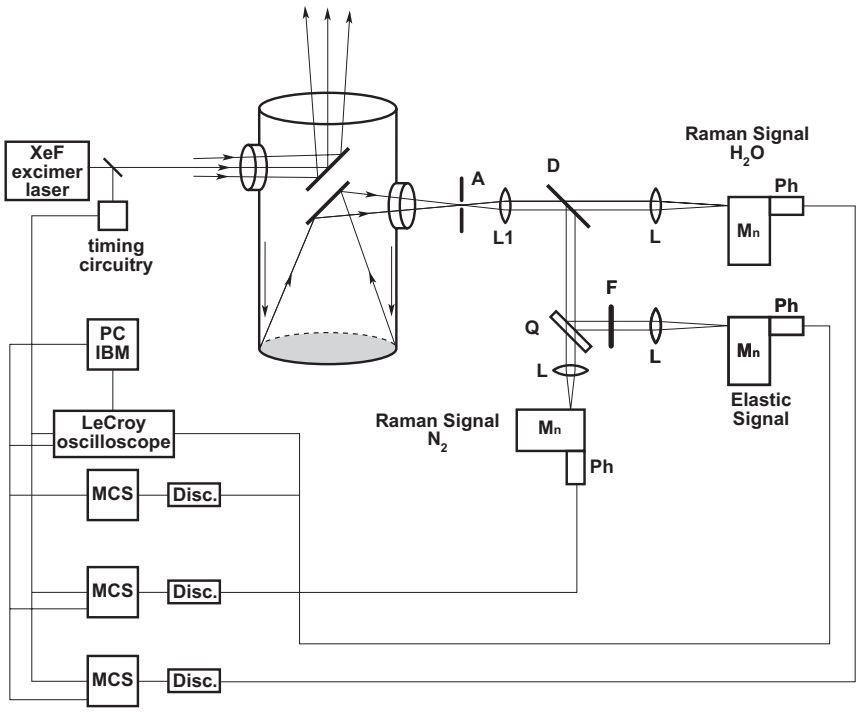

Fig. 1, De Tomasi and Perrone

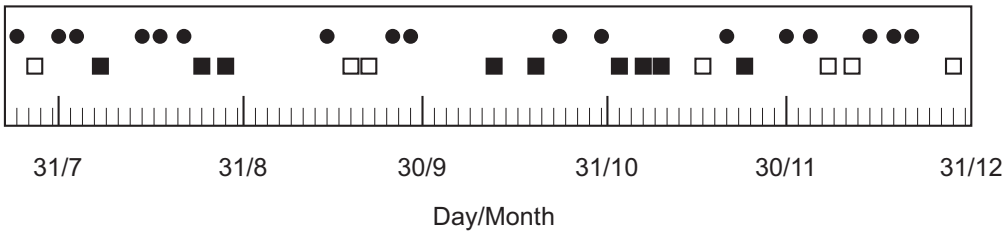

Fig. 2, De Tomasi and Perrone

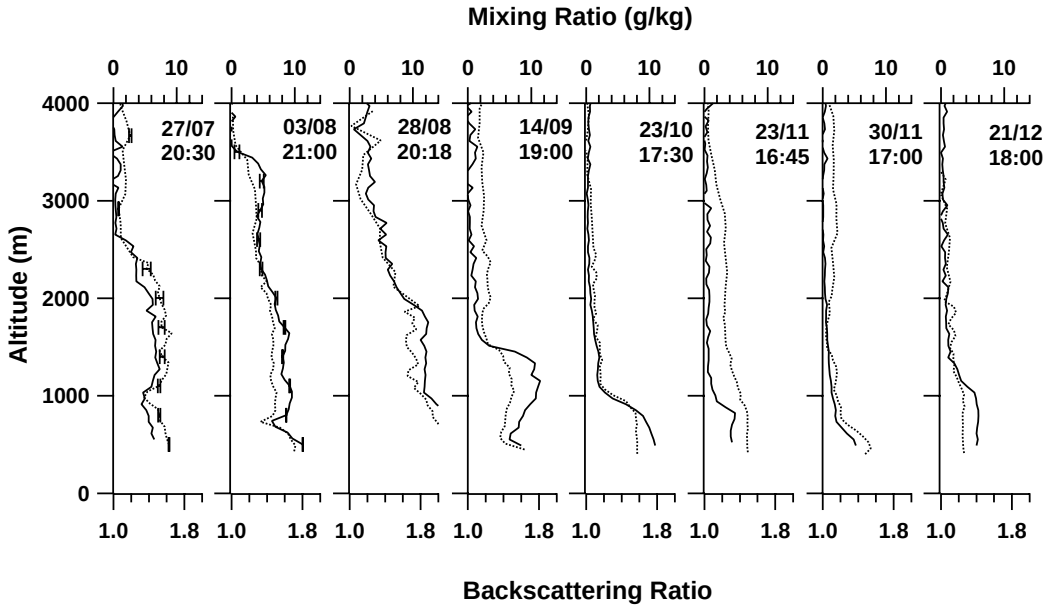

Fig. 3, De Tomasi and Perrone

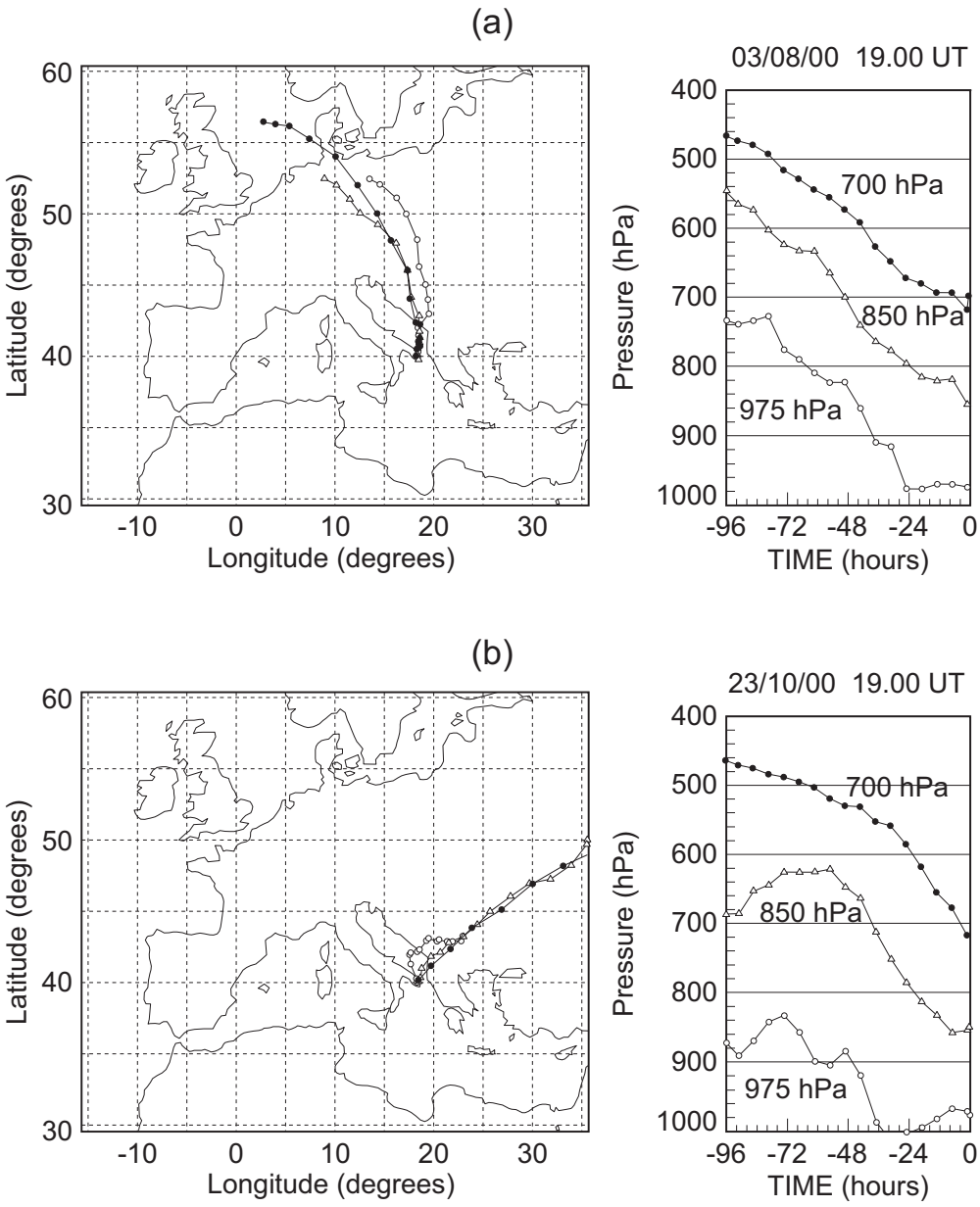

Fig. 4, De Tomasi and Perrone

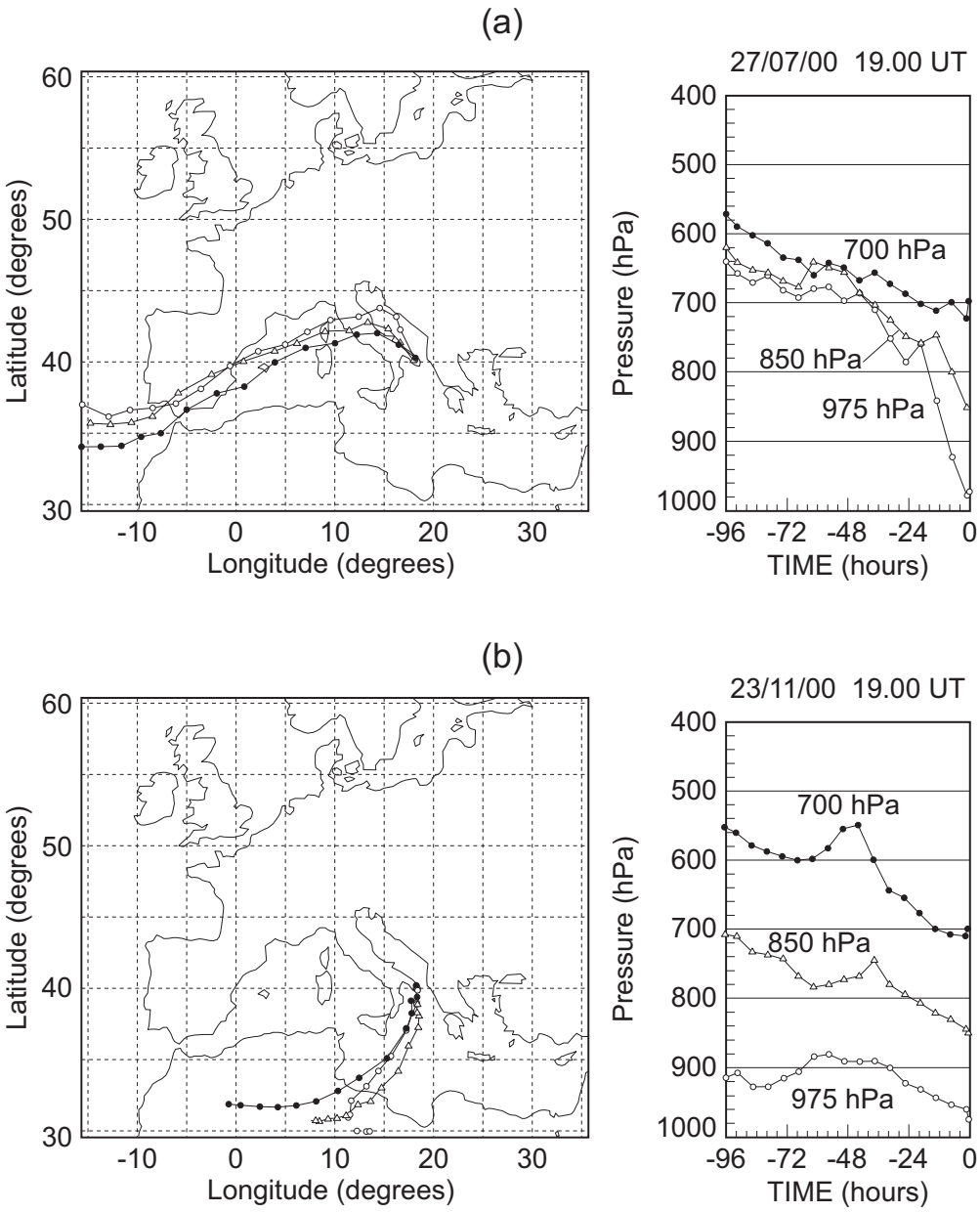

Fig. 5, De Tomasi and Perrone

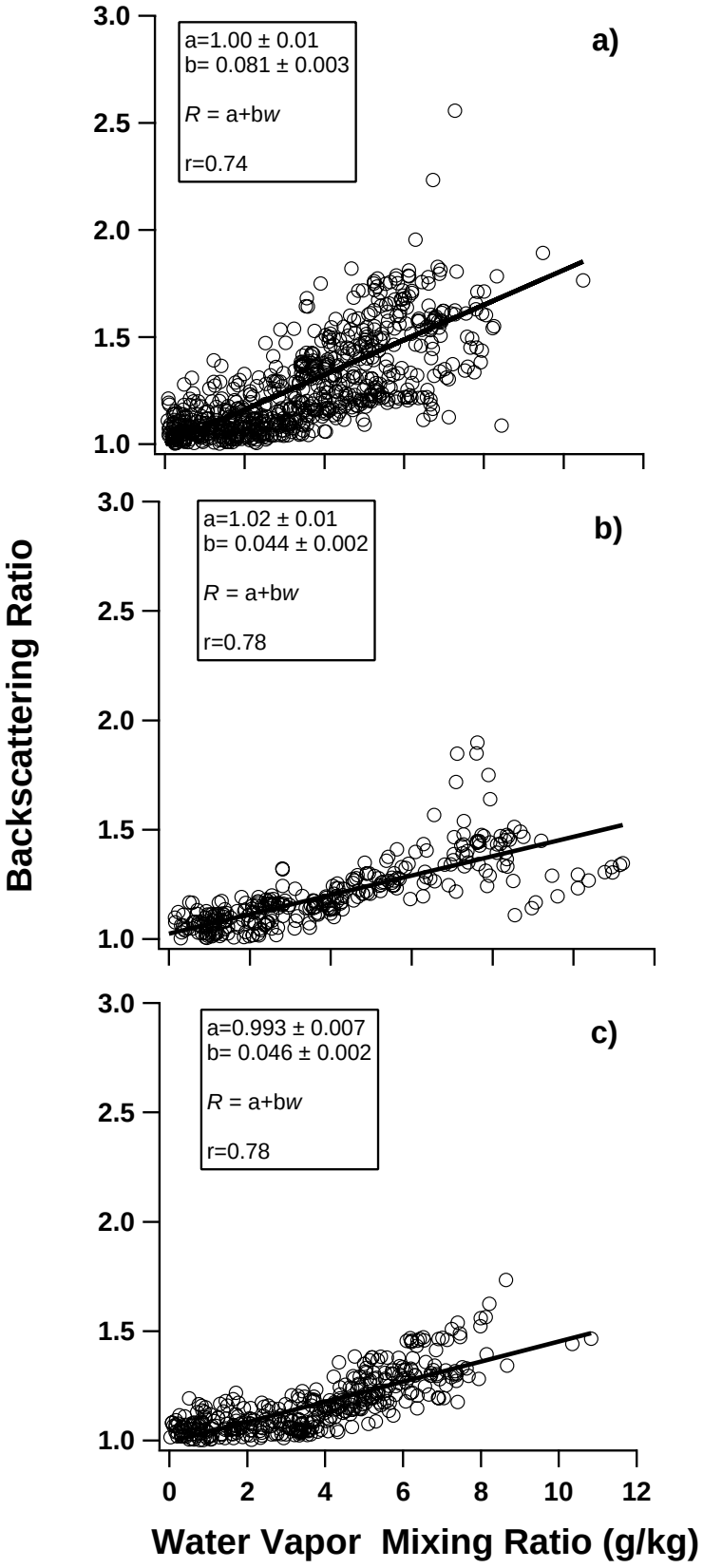

Fig. 6 De Tomasi and Perrone

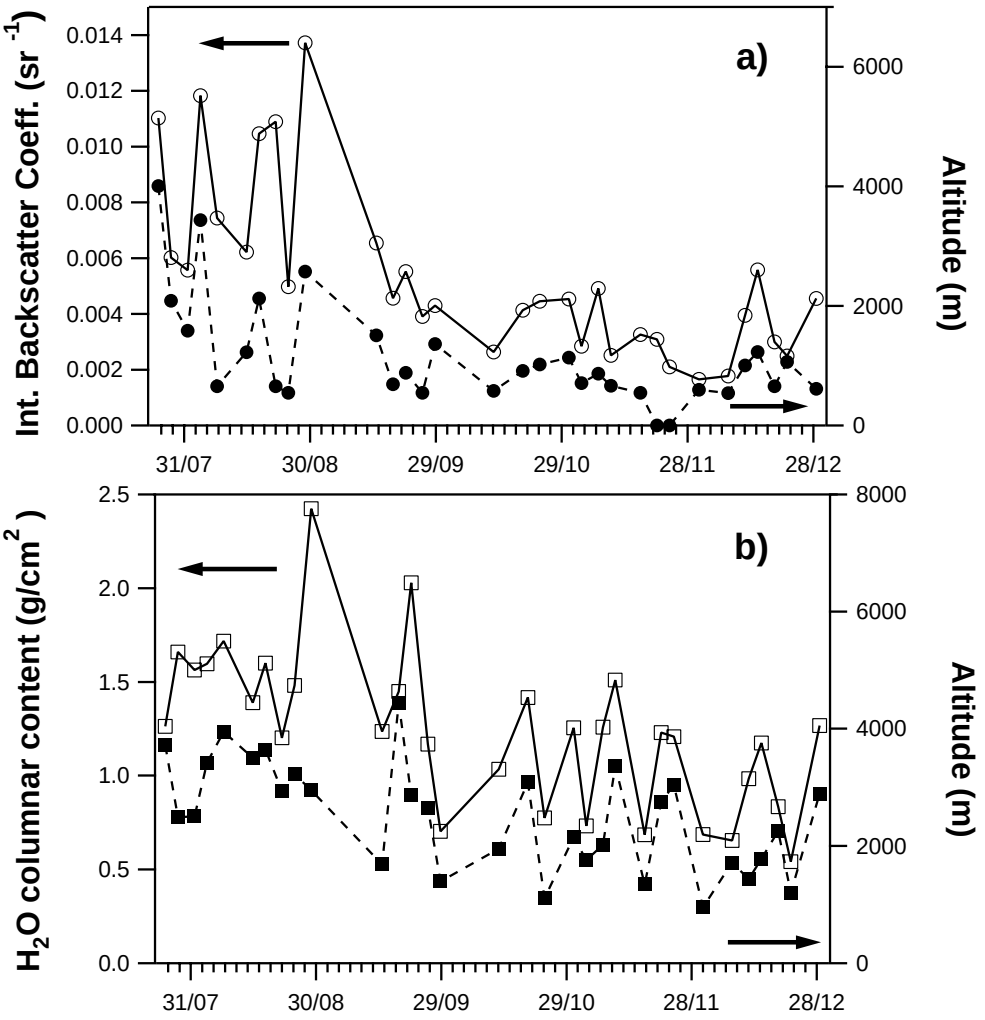

Fig. 7, De Tomasi and Perrone

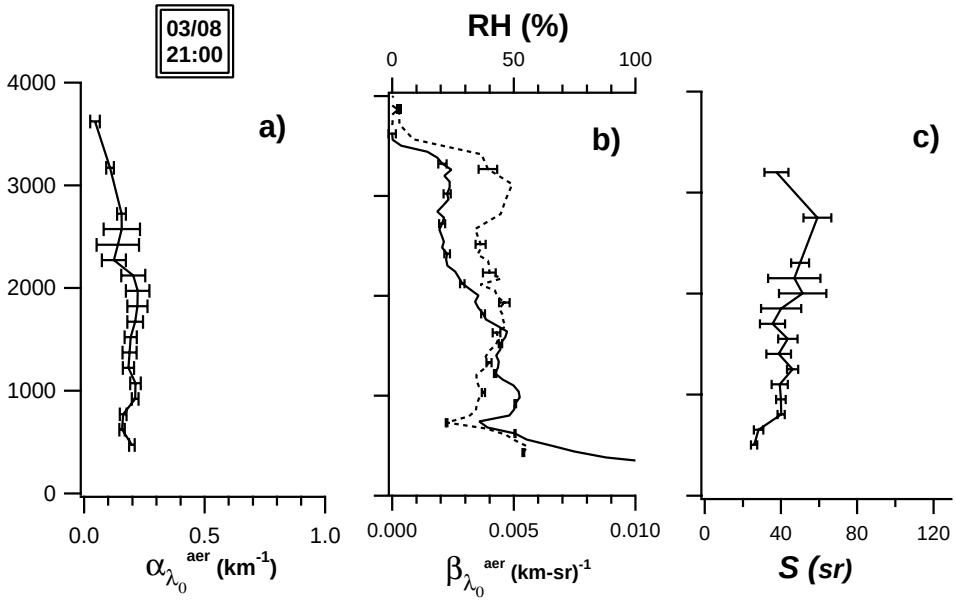

Fig. 8, De Tomasi and Perrone

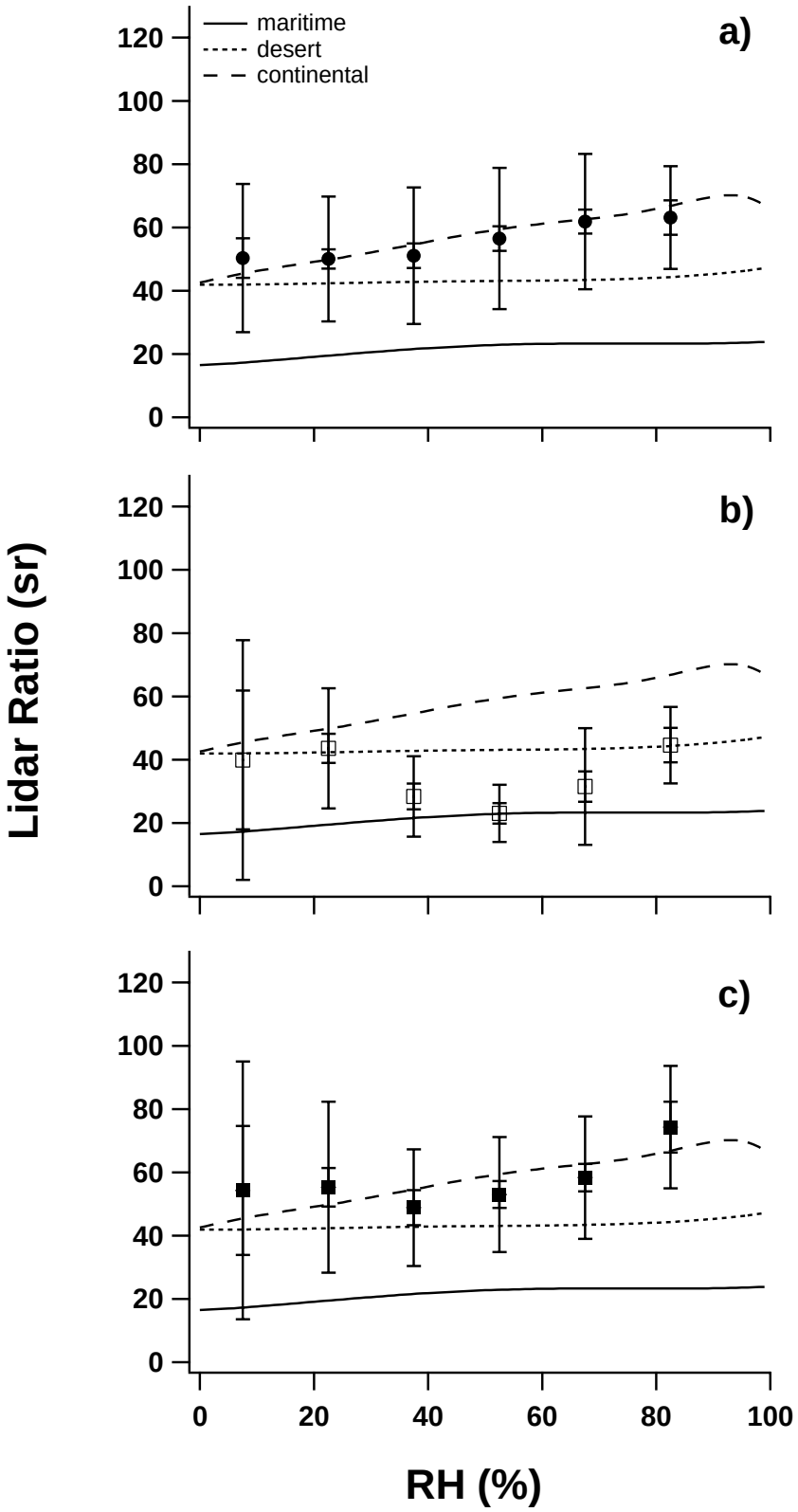

Fig.9 De Tomasi and Perrone